LETTER

Elucidation of the Fe(IV)=O intermediate in the catalytic cycle of the halogenase SyrB2

Shaun D. Wong[1]*, Martin Srnec[1]*, Megan L. Matthews[2]†, Lei V. Liu[1], Yeonju Kwak[1], Kiyoung Park[1], Caleb B. Bell III[1], E. Ercan Alp[3], Jiyong Zhao[3], Yoshitaka Yoda[4], Shinji Kitao[5], Makoto Seto[5], Carsten Krebs[2,6], J. Martin Bollinger Jr[2,6] & Edward I. Solomon[1,7]

Mononuclear non-haem iron (NHFe) enzymes catalyse a broad range of oxidative reactions, including halogenation, hydroxylation, ring closure, desaturation and aromatic ring cleavage reactions. They are involved in a number of biological processes, including phenylalanine metabolism, the production of neurotransmitters, the hypoxic response and the biosynthesis of secondary metabolites[1–3]. The reactive intermediate in the catalytic cycles of these enzymes is a high-spin $S = 2$ Fe(IV)=O species, which has been trapped for a number of NHFe enzymes[4–8], including the halogenase SyrB2 (syringomycin biosynthesis enzyme 2). Computational studies aimed at understanding the reactivity of this Fe(IV)=O intermediate[9–13] are limited in applicability owing to the paucity of experimental knowledge about its geometric and electronic structure. Synchrotron-based nuclear resonance vibrational spectroscopy (NRVS) is a sensitive and effective method that defines the dependence of the vibrational modes involving Fe on the nature of the Fe(IV)=O active site[14–16]. Here we present NRVS structural characterization of the reactive Fe(IV)=O intermediate of a NHFe enzyme, namely the halogenase SyrB2 from the bacterium *Pseudomonas syringae* pv. *syringae*. This intermediate reacts via an initial hydrogen-atom abstraction step, performing subsequent halogenation of the native substrate or hydroxylation of non-native substrates[17]. A correlation of the experimental NRVS data to electronic structure calculations indicates that the substrate directs the orientation of the Fe(IV)=O intermediate, presenting specific frontier molecular orbitals that can activate either selective halogenation or hydroxylation.

SyrB2, an α-ketoglutarate (αKG)-dependent NHFe enzyme found in *Pseudomonas syringae* pv. *syringae*, halogenates the methyl group of L-threonine (L-Thr) using non-ribosomal peptide synthetase machinery[18]. The Fe(II) active site is ligated by two histidines and one halide (Cl⁻ or Br⁻) (see Supplementary Fig. 1)[19], in contrast to the two-histidine/one-carboxylate 'facial triad' of other NHFe enzymes[1,2,4,5,8]. Although the mechanisms of O₂ activation leading to the highly-reactive $S = 2$ Fe(IV)=O intermediate are thought to be similar for all αKG-dependent NHFe enzymes, there is a notable divergence in their subsequent catalytic cycles (Fig. 1). The Fe(IV)=O species abstracts a hydrogen atom from the substrate to form an Fe(III)–OH species and a substrate radical; in hydroxylases, the subsequent step is HO• rebound to form a hydroxylated product[1,2], but in SyrB2 the native L-Thr substrate is chlorinated instead, and the 4-Cl-L-Thr product is used in the biosynthesis of the phytotoxin syringomycin E[18]. Owing to their reactivity, Fe(IV)=O intermediates in enzyme reactions are challenging to trap and characterize. For SyrB2, however, use of the non-native substrate L-cyclopropylglycine (L-Cpg) and the heterologous substrate carrier protein CytC2 has provided a long-lived species at the concentrations required for spectroscopic investigation[17,20].

Nuclear resonance vibrational spectroscopy (NRVS) utilizes third-generation synchrotron radiation to probe the vibrational sidebands of the ⁵⁷Fe Mössbauer nuclear resonance peak at 14.4 keV (refs 21–23). NRVS is a site-selective technique allowing the observation of only normal modes involving Fe motion, which makes it ideal for studying iron-dependent enzymes without interference from protein backbone modes. (SyrB2)Fe(IV)=O can be generated in high purity with both Cl⁻ and Br⁻ ligation of the Fe(IV)=O unit, providing a mass perturbation that aids in the assignment of NRVS peaks and ultimately the structure of the intermediate. The NRVS methodology is coupled with spectroscopically calibrated density functional theory (DFT) calculations to evaluate specific frontier molecular orbitals (FMOs) responsible for hydrogen-atom abstraction that can selectively lead to halogenation or hydroxylation, depending on the substrate.

In Fig. 2 we show the NRVS partial vibrational density-of-states (PVDOS) spectra of (SyrB2)Cl–Fe(IV)=O with L-Cpg–S–CytC2 bound (referred to as SyrB2–Cl) and the bromide analogue, (SyrB2)Br–Fe(IV)=O with L-Cpg–S–CytC2 bound (SyrB2–Br). For practical reasons (see Methods), data collection was restricted to <600 cm⁻¹; modes in this region are affected by large (Cl versus Br; see below) but not small (¹⁶O versus ¹⁸O; see Supplementary Fig. 2) mass perturbations. There are three distinct features for each species, as indicated by the bracketed energy regions: region 1 (340–400 cm⁻¹), region 2 (285–340 cm⁻¹) and region 3 (200–285 cm⁻¹). For the higher-energy regions 1 and 2, the
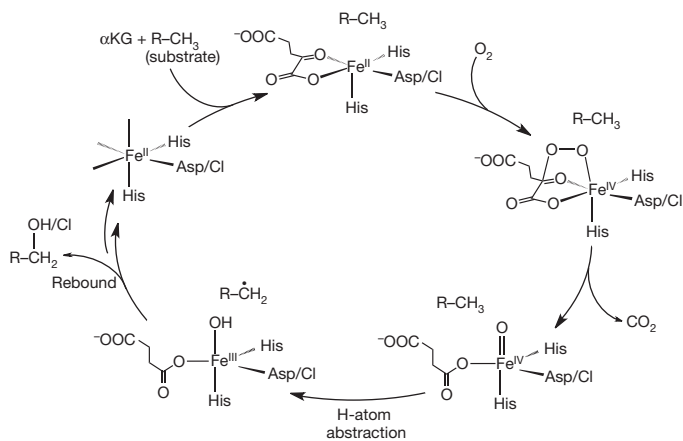

Figure 1 | Catalytic cycle of αKG-dependent NHFe enzymes. αKG and substrate binding induces a six-coordinate to five-coordinate conversion (top), providing a site for O₂ to bind and form an Fe(IV)–peroxo species that nucleophilically attacks αKG, producing a peroxo-bridged Fe(IV) species (right)[24]. Decarboxylation of αKG leads to the reactive Fe(IV)=O intermediate (bottom right), which goes on to perform hydrogen-atom abstraction (bottom left) and subsequent rebound hydroxylation or halogenation.

[1]Department of Chemistry, Stanford University, Stanford, California 94305, USA. [2]Department of Chemistry, Pennsylvania State University, University Park, Pennsylvania 16802, USA. [3]Argonne National Laboratory, APS/XFD, 431/D003, Argonne, Illinois 60439, USA. [4]SPring-8, JASRI, Hyogo 679-5198, Japan. [5]Research Reactor Institute, Kyoto University, Osaka 590-0494, Japan. [6]Department of Biochemistry and Molecular Biology, Pennsylvania State University, University Park, Pennsylvania 16802, USA. [7]SLAC National Accelerator Laboratory, Menlo Park, California 94025, USA. †Present address: Department of Chemical Physiology, The Scripps Research Institute, La Jolla, California 92307, USA.
*These authors contributed equally to this work.

peaks of SyrB2–Cl are more intense. However, for the low-energy region 3, the peak envelope for SyrB2–Br is considerably more intense and shifted to lower energy.

Previous computational studies of the Cl–Fe(IV)=O intermediate of SyrB2 predicted six-coordinate structures with the succinate bound as a bidentate ligand to Fe (refs 9–12). The DFT-calculated NRVS spectra of these six-coordinate structures (Supplementary Fig. 3) do not reproduce the splitting pattern and intensity distribution of the experimental data, and can thus be eliminated from consideration.

To generate and evaluate suitable structural candidates, the O_2 reaction coordinate taking SyrB2 to its Fe(IV)=O intermediate (Fig. 1) was investigated using DFT calculations. The initial structure was taken from the crystal structure of the SyrB2 Fe(II) active site with the αKG cofactor and Cl$^-$ bound (Supplementary Fig. 1)[19] and the native substrate L-Thr positioned according to a molecular docking procedure[12]; its side chain was also modified into the non-native substrate L-Cpg to generate a second starting structure. Application of the spectroscopically calibrated DFT methodology used for a related αKG-dependent mononuclear NHFe enzyme[24] resulted in an equivalent O_2 reaction coordinate for the Fe(II) active site of SyrB2 (Supplementary Figs 4 and 5a, b).

This O_2 reaction coordinate leads to 1_{Cpg}–Cl (Fig. 3b) and 1_{Thr}–Cl (Supplementary Fig. 5b) with L-Cpg and L-Thr respectively; both are five-coordinate trigonal bipyramidal (TBP) Fe(IV)=O structures possessing an axial oxo group and a monodentate succinate. Significantly, in both cases, the Fe–oxo vector is oriented perpendicularly to the target substrate C–H bond, with interesting implications for π-channel reactivity[25,26].

1_{Cpg}–Cl was evaluated as a structural candidate for the Fe(IV)=O intermediate in the NRVS sample. The geometry-optimized Fe–oxo and Fe–Cl bond lengths (Fig. 3b) of 1_{Cpg}–Cl are in close agreement with the experimental extended X-ray absorption fine structure (EXAFS) values (1.66 Å and 2.31 Å respectively)[7]. The Br$^-$ cognate, 1_{Cpg}–Br, was generated by replacing Cl$^-$ with Br$^-$ and reoptimizing the structure; its Fe–Br bond length of 2.45 Å (Fig. 3b) agrees well with the EXAFS value of 2.43 Å for the related halogenase CytC3 (ref. 6). Thus, these five-coordinate TBP intermediates 1_{Cpg}–X (X = Cl or Br) resulting from the O_2 reaction coordinate were used for comparison with the experimental NRVS data on the SyrB2 Fe(IV)=O intermediates SyrB2–X.

As seen in Fig. 3, the five-coordinate TBP species 1_{Cpg}–X result in DFT-predicted spectra that reproduce the experimental spectra. First,
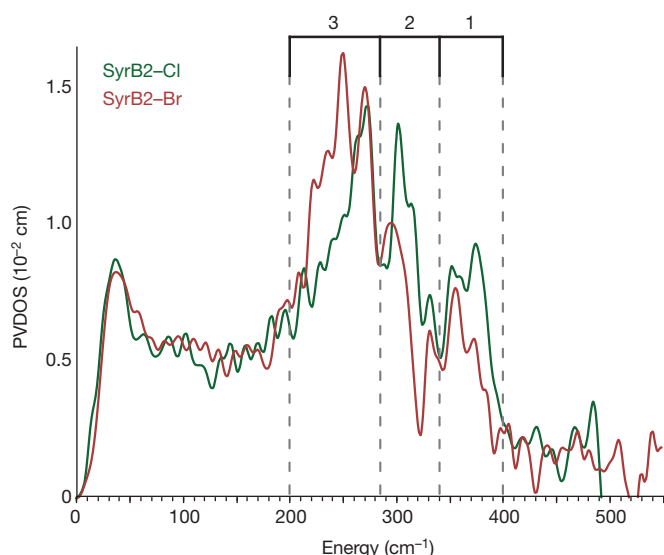
there are three distinct peaks falling within the energy regions of 200–285 cm^{-1}, 285–340 cm^{-1} and 340–400 cm^{-1}, matching regions 3, 2 and 1 in Fig. 2. Second, the intensities of the peaks in the two higher-energy regions are greater for 1_{Cpg}–Cl than for 1_{Cpg}–Br, and the intensity of the peak envelope in the lowest-energy region for 1_{Cpg}–Br is greater and shifted to lower energy with respect to that of 1_{Cpg}–Cl, reproducing the spectral intensity distributions of the experimental data (Fig. 2). Other five- and six-coordinate structures were generated as possible candidates for the Fe(IV)=O species, starting from 1_{Cpg}–X and shifting either the Fe-ligating atoms or the hydrogen-bonding network to the oxo group (Supplementary Fig. 6). From the predicted NRVS spectra of these structures and of the structures generated in previous (computational) studies (Supplementary Fig. 3), all structures except five-coordinate TBP can be eliminated owing to their poor agreement with the experimental NRVS data.

Correlating the DFT-calculated spectra of five-coordinate TBP 1_{Cpg}–X (Fig. 3) with the experimental spectra (Fig. 2), the NRVS peaks can be assigned to four normal modes (Fig. 4): the feature in region 1 (Fig. 2) originates from the Fe–succinate stretch; the feature in region 2 is composed of a pair of *trans*-axial bending modes (these would be degenerate in strict TBP symmetry, but are calculated to split in energy because of the wider equatorial X–Fe–succinate angle of 143°)[15]; the
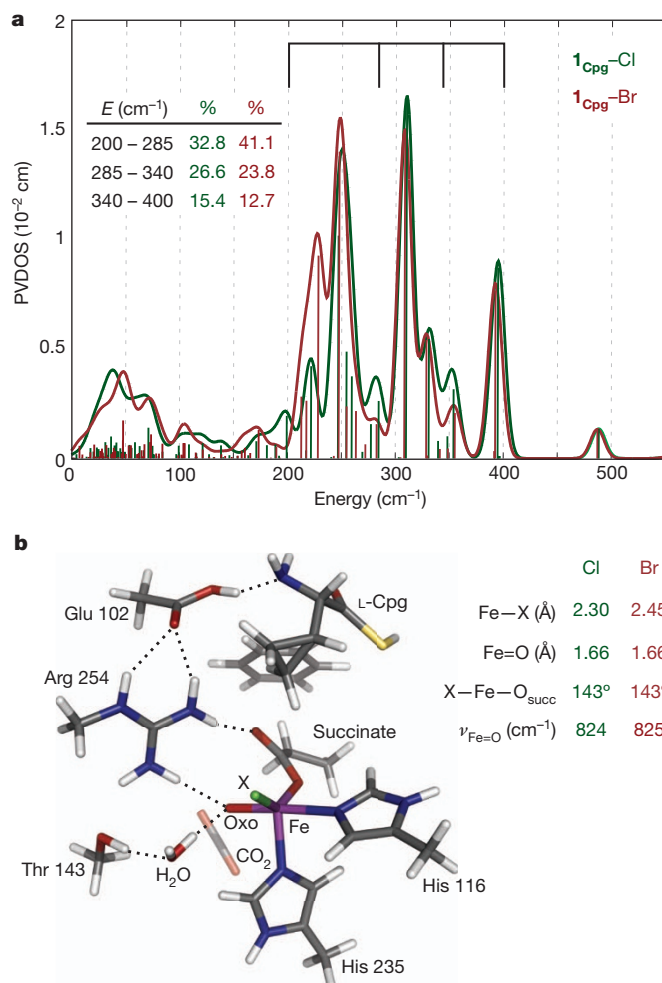

Figure 2 | **NRVS PVDOS spectra of SyrB2–Cl and SyrB2–Br.** Regions 3, 2 and 1 that contain intense features are indicated at the top.

Figure 3 | **Computational spectra and structure of five-coordinate TBP structural candidate** 1_{Cpg}–X **for the Fe(IV)=O intermediate of SyrB2.** **a**, DFT-predicted PVDOS NRVS spectra. Vertical bars represent relative calculated mode-composition factors of vibrational modes, and brackets at top correspond to energy regions from Fig. 2. Inset, peak intensity contributions (from the three bracketed regions) to the overall PVDOS envelope. **b**, Structure of 1_{Cpg}–X (left), along with geometric parameters and Fe–oxo stretching frequencies (right).

lowest-energy region 3 has a peak envelope calculated to contain the *trans*-axial stretch and the Fe–X stretch, with the Fe–Br stretch being lower in energy by $30\,cm^{-1}$ and more intense by 1.5 times. The redistribution in intensity is attributed to the mass perturbation of the Br, which has almost no motion in the Fe–X stretching mode and consequently induces greater Fe motion in the mode. This Fe motion is borrowed from higher-energy modes, as analysed in Supplementary Fig. 7. The NRVS peak pattern of SyrB2–X parallels that of a crystallographically characterized TBP $S = 2$ Fe(IV)=O model complex (Supplementary Fig. 8)[15], further demonstrating the sensitivity of NRVS to geometric structure.

We note that two distinct Fe(IV) species are detected by Mössbauer spectroscopy, differing in quadrupole splitting, ΔE_Q (Supplementary Fig. 9), in each Fe(IV)=O intermediate generated[7]. A possible explanation for this speciation lies in the hydrogen-bonding interactions with the oxo group: 1_{Cpg}–Cl has two (with Arg 254 and H_2O), whereas 1_{Thr}–Cl has one (with H_2O). Their predicted NRVS spectra are similar (Supplementary Figs 6 and 10a), but their calculated values of ΔE_Q are different, with that of 1_{Cpg}–Cl ($-0.50\,mm\,s^{-1}$) being smaller in magnitude than that of 1_{Thr}–Cl ($-0.71\,mm\,s^{-1}$). Decreasing the number of hydrogen bonds strengthens the Fe–oxo bond, thus increasing the magnitude of (negative) ΔE_Q (Supplementary Fig. 10a and Supplementary Table 1). These calculations suggest that variability in hydrogen-bonding interactions with the oxo group results in Fe(IV) speciation, not some structural difference.

For the native L-Thr substrate (starting from the O_2-reaction-coordinate-derived Fe(IV)=O species 1_{Thr}–Cl, which has its Fe–oxo vector perpendicular to C–H (Supplementary Fig. 5b)) the hydrogen-atom abstraction reactivity was computationally evaluated (Fig. 5). The target C–H approaches in a π-trajectory, transferring an α-electron into the oxo π-FMO, resulting in an Fe(III)–OH first product (1_{Thr}–Fe(III)OH), in which the Fe(III) has spin $S = 5/2$. The free-energy barrier $\Delta G^{\ddagger}$ for this π-pathway is $+100.4\,kJ\,mol^{-1}$, in reasonable agreement with the experimental value of $+79.4\,kJ\,mol^{-1}$ (ref. 7). A number of possible explanations have been considered for the subsequent Cl• rebound[17,27]; here we show that in this first product, the substrate radical is positioned closer to the Cl than to the OH ligand of Fe(III) (consideration of their ionic radii places Cl 0.5 Å closer than OH), and OH is also stabilized by hydrogen-bonding to succinate (Fig. 5, right). This conformation disfavours HO• rebound but is well oriented for Cl• rebound, as observed experimentally with the native substrate. This perpendicular Fe–oxo orientation is, for the six-coordinate structures proposed in previous computational studies[9–12], inaccessible via the O_2-activation pathway because a bidentate succinate would block the oxo group from reorienting.

Evaluation of the reaction coordinate for O–O cleavage leading to the Fe(IV)=O species (Supplementary Fig. 5) revealed that the positioning of L-Thr is fixed by two hydrogen-bonding interactions ($-OH$ and $-NH_3^+$) to Glu 102. This configuration results in the perpendicular orientation of the Fe(IV)–oxo vector relative to the substrate C–H bond. However, the alternative substrate L-norvaline (L-Nva) lacks the $-OH$ group, and thus its $-NH_3^+$ group can rotate to form a hydrogen bond with the O–O (peroxy) bridge, leading to a structure with an
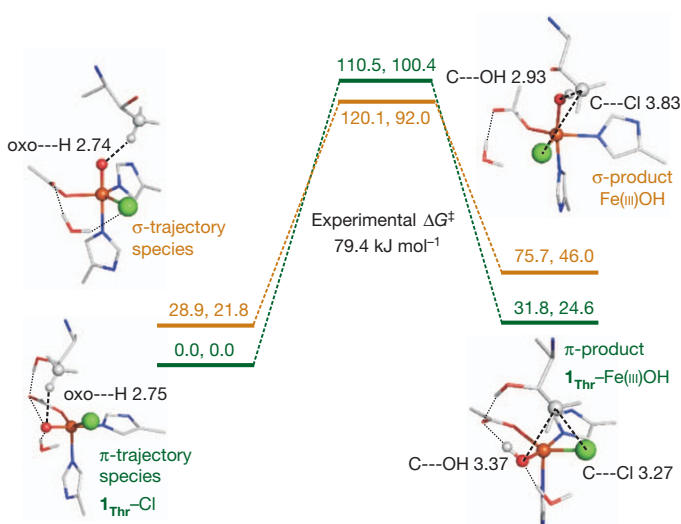
Figure 5 | Hydrogen-atom abstraction reaction coordinates. Energies (given as ΔE, ΔG in $kJ\,mol^{-1}$) for the π-trajectory (1_{Thr}–Cl, green numerals and levels) and the σ-trajectory (orange numerals and levels) are shown. Reactants are on the left; energies for the transition state (where the Fe has developed $S = 5/2$ spin character) are given at the top; structures of Fe(III)–OH products (in which the Fe(III) has spin $S = 5/2$) are displayed on the right, showing the π-product 1_{Thr}–Fe(III)–OH (with hydrogen-bonding interactions indicated) set up for chlorination and the σ-product set up for hydroxylation. Distances are given in Å. For additional structural details, see Supplementary Fig. 11.

Fe–oxo vector oriented towards the substrate C–H bond (Supplementary Fig. 5c). An analogous L-Thr orientation was thus generated to evaluate its hydrogen-atom abstraction trajectory while maintaining the same C–H bond (Fig. 5, left).

For this orientation, the C–H approaches the Fe–oxo unit in a σ-trajectory, transferring an α-electron into the oxo σ-FMO to give an Fe(III)–OH product in which the Fe(III) has spin $S = 5/2$; this σ-pathway has a $\Delta G^{\ddagger}$ of $+70.2\,kJ\,mol^{-1}$ (Fig. 5). Relative to the π-pathway Fe(III)–OH product, this Fe(III)–OH has the substrate radical closer to the OH ligand than the Cl (by 0.5 Å, based on ionic radii), and OH has no hydrogen-bonding partner. The parallel Fe–oxo orientation therefore favours HO• rebound, as is observed experimentally for the non-native substrate L-Nva[17]. We also note that the barrier for π-attack is somewhat higher than that for σ-attack, which is consistent with the higher barrier observed experimentally for halogenation relative to hydroxylation (by $\sim 17\,kJ\,mol^{-1}$)[17], reflecting halogenation selectivity over efficiency.

We have used NRVS to characterize the NHFe enzyme oxo intermediate in SyrB2 and found the Fe to be in a five-coordinate TBP configuration, with an axial Fe(IV)=O bond. The native-substrate-bound O_2 reaction coordinate reproduces this structure and gives an intermediate with its Fe–oxo vector perpendicular to the substrate C–H bond; this Fe–oxo orientation is active in hydrogen-atom abstraction, via its π*-FMO. This positions the substrate radical favourably for Cl• rebound, thus defining a selective mechanism in halogenases for chlorination of the native substrate. Alternatively, with a non-native substrate, variation in the O_2 reaction coordinate can lead to an intermediate with its Fe–oxo vector parallel to the substrate C–H bond, leading to hydrogen-atom abstraction via a σ-pathway and a substrate radical positioned for HO• rebound and resultant hydroxylation.

METHODS SUMMARY

Sample preparation. Samples were prepared essentially as previously described[7]. Details of experimental conditions (such as concentrations) are provided in Supplementary Fig. 9.

Spectroscopic methods. ^{57}Fe NRVS spectra were recorded on multiple occasions at Beamline 3-ID at the Advanced Photon Source of the Argonne National Laboratory[28], at temperatures between 10 K and 30 K, and once at BL09XU at
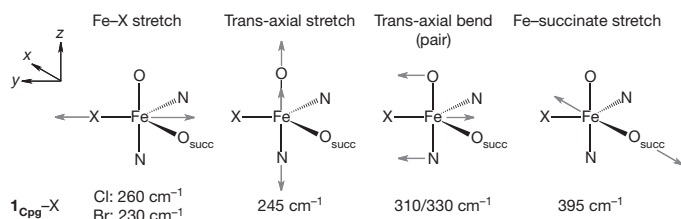

Figure 4 | DFT-predicted normal modes of 1_{Cpg}–X. Four normal modes of the five-coordinate TBP Fe(IV)=O structure are shown; above are the mode descriptions, below are the corresponding frequencies. The Fe–oxo vector defines the z axis.

SPring-8 in Japan[29], at temperatures between 50 K and 80 K. NRVS data were collected only up to 600 cm^{-1} owing to relatively low sample concentrations (~1.8 mM); because NRVS signal intensity decreases exponentially with increasing energy, data collected above this region (given our allocated beamtime) would have had a low signal-to-noise ratio.

Computational methods. DFT methods were used to simulate the NRVS spectra and Mössbauer parameters of all structural candidates, and to evaluate the hydrogen-atom abstraction reaction coordinates (see Methods).

Full Methods and any associated references are available in the online version of the paper.

1. Solomon, E. I. *et al.* Geometric and electronic structure/function correlations in non-heme iron enzymes. *Chem. Rev.* **100,** 235–350 (2000).
2. Costas, M., Mehn, M. P., Jensen, M. P. & Que, L. Jr. Dioxygen activation at mononuclear nonheme iron active sites: enzymes, models, and intermediates. *Chem. Rev.* **104,** 939–986 (2004).
3. Vaillancourt, F. H., Yeh, E., Vosburg, D. A., Garneau-Tsodikova, S. & Walsh, C. T. Nature's inventory of halogenation catalysts: oxidative strategies predominate. *Chem. Rev.* **106,** 3364–3378 (2006).
4. Krebs, C., Galonić Fujimori, D., Walsh, C. T. & Bollinger, J. M. Jr. Non-heme Fe(IV)-oxo intermediates. *Acc. Chem. Res.* **40,** 484–492 (2007).
5. Eser, B. E. *et al.* Direct spectroscopic evidence for a high-spin Fe(IV) intermediate in tyrosine hydroxylase. *J. Am. Chem. Soc.* **129,** 11334–11335 (2007).
6. Galonić Fujimori, D. *et al.* Spectroscopic evidence for a high-spin Br-Fe(IV)-oxo intermediate in the alpha-ketoglutarate-dependent halogenase CytC3 from *Streptomyces. J. Am. Chem. Soc.* **129,** 13408–13409 (2007).
7. Matthews, M. L. *et al.* Substrate-triggered formation and remarkable stability of the C−H bond-cleaving chloroferryl intermediate in the aliphatic halogenase, SyrB2. *Biochemistry* **48,** 4331–4343 (2009).
8. Panay, A. J., Lee, M., Krebs, C., Bollinger, J. M. Jr & Fitzpatrick, P. F. Evidence for a high-spin Fe(IV) species in the catalytic cycle of a bacterial phenylalanine hydroxylase. *Biochemistry* **50,** 1928–1933 (2011).
9. Pandian, S., Vincent, M. A., Hillier, I. H. & Burton, N. A. Why does the enzyme SyrB2 chlorinate, but does not hydroxylate, saturated hydrocarbons? A density functional theory (DFT) study. *Dalton Trans.* 6201–6207 (2009).
10. Kulik, H. J., Blasiak, L. C., Marzari, N. & Drennan, C. L. First-principles study of non-heme Fe(II) halogenase SyrB2 reactivity. *J. Am. Chem. Soc.* **131,** 14426–14433 (2009).
11. de Visser, S. P. & Latifi, R. Carbon dioxide: a waste product in the catalytic cycle of alpha-ketoglutarate dependent halogenases prevents the formation of hydroxylated by-products. *J. Phys. Chem. B* **113,** 12–14 (2009).
12. Borowski, T., Noack, H., Radoń, M., Zych, K. & Siegbahn, P. E. M. Mechanism of selective halogenation by SyrB2: a computational study. *J. Am. Chem. Soc.* **132,** 12887–12898 (2010).
13. Usharani, D., Janardanan, D. & Shaik, S. Does the TauD enzyme always hydroxylate alkanes, while an analogous synthetic non-heme reagent always desaturates them? *J. Am. Chem. Soc.* **133,** 176–179 (2011).
14. Bell, C. B. *et al.* A combined NRVS and DFT study of Fe^{IV}=O model complexes: a diagnostic method for the elucidation of non-heme iron enzyme intermediates. *Angew. Chem. Int. Edn* **47,** 9071–9074 (2008).
15. Wong, S. D. *et al.* Nuclear resonance vibrational spectroscopy on the Fe^{IV}=O S = 2 non-heme site in TMG$_3$tren: experimentally calibrated insights into reactivity. *Angew. Chem. Int. Edn* **50,** 3215–3218 (2011).
16. Park, K. *et al.* Nuclear resonance vibrational spectroscopic and computational study of high-valent diiron complexes relevant to enzyme intermediates. *Proc. Natl Acad. Sci. USA* **110,** 6275–6280 (2013).
17. Matthews, M. L. *et al.* Substrate positioning controls the partition between halogenation and hydroxylation in the aliphatic halogenase, SyrB2. *Proc. Natl Acad. Sci. USA* **106,** 17723–17728 (2009).
18. Vaillancourt, F. H., Yin, J. & Walsh, C. T. SyrB2 in syringomycin E biosynthesis is a nonheme Fe^{II} α-ketoglutarate- and O$_2$-dependent halogenase. *Proc. Natl Acad. Sci. USA* **102,** 10111–10116 (2005).
19. Blasiak, L. C., Vaillancourt, F. H., Walsh, C. T. & Drennan, C. L. Crystal structure of the non-haem iron halogenase SyrB2 in syringomycin biosynthesis. *Nature* **440,** 368–371 (2006).
20. Krebs, C. *et al.* Novel approaches for the accumulation of oxygenated intermediates to multi-millimolar concentrations. *Coord. Chem. Rev.* **257,** 234–243 (2013).
21. Seto, M., Yoda, Y., Kikuta, S., Zhang, X. & Ando, M. Observation of nuclear resonant scattering accompanied by phonon excitation using synchrotron radiation. *Phys. Rev. Lett.* **74,** 3828–3831 (1995).
22. Chumakov, A. I. & Sturhahn, W. Experimental aspects of inelastic nuclear resonance scattering. *Hyperfine Interact.* **123/124,** 781–808 (1999).
23. Sage, J. T. *et al.* Nuclear resonance vibrational spectroscopy of a protein active-site mimic. *J. Phys. Condens. Matter* **13,** 7707–7722 (2001).
24. Diebold, A. R. *et al.* Activation of α-keto acid-dependent dioxygenases: application of an {FeNO}^{7}/{FeO$_2$}^{8} methodology for characterizing the initial steps of O$_2$ activation. *J. Am. Chem. Soc.* **133,** 18148–18160 (2011).
25. Neidig, M. L. *et al.* Spectroscopic and electronic structure studies of aromatic electrophilic attack and hydrogen-atom abstraction by non-heme iron enzymes. *Proc. Natl Acad. Sci. USA* **103,** 12966–12973 (2006).
26. Srnec, M., Wong, S. D., England, J., Que, L. & Solomon, E. I. π-frontier molecular orbitals in S = 2 ferryl species and elucidation of their contributions to reactivity. *Proc. Natl Acad. Sci. USA* **109,** 14326–14331 (2012).
27. Comba, P. & Wunderlich, S. Iron-catalyzed halogenation of alkanes: modeling of nonheme halogenases by experiment and DFT calculations. *Chemistry* **16,** 7293–7299 (2010).
28. Alp, E. E., Mooney, T. M., Toellner, T. & Sturhahn, W. Nuclear resonant scattering beamline at the Advanced Photon Source. *Hyperfine Interact.* **90,** 323–334 (1994).
29. Yoda, Y. *et al.* Nuclear resonant scattering beamline at SPring-8. *Nucl. Instrum. Methods A* **467–468,** 715–718 (2001).

Author Contributions S.D.W. and M. Srnec contributed equally to this work. E.I.S., C.K. and J.M.B. designed the experiments. S.D.W., M. Srnec, M.L.M., L.V.L., Y.K., K.P. and C.B.B. performed the experiments. S.D.W., M. Srnec and E.I.S. analysed the data and wrote the manuscript. E.E.A., J.Z., Y.Y., S.K. and M. Seto provided technical assistance at the sychrotron beamlines.

Author Information Reprints and permissions information is available at www.nature.com/reprints. The authors declare no competing financial interests. Readers are welcome to comment on the online version of the paper. Correspondence and requests for materials should be addressed to C.K. (ckrebs@psu.edu), J.M.B. (jmb21@psu.edu) or E.I.S. (edward.solomon@stanford.edu).

METHODS

Sample preparation. Samples were prepared essentially as previously described[7]. Details of experimental conditions (such as concentrations) are provided in Supplementary Fig. 9.

Spectroscopic methods. [57]Fe NRVS spectra were recorded on multiple occasions at Beamline 3-ID at the Advanced Photon Source of the Argonne National Laboratory[28], at temperatures between 10 K and 30 K, and once at BL09XU at SPring-8 in Japan[29], at temperatures between 50 K and 80 K. NRVS data were collected only up to 600 cm^{-1} owing to relatively low sample concentrations (~1.8 mM); because NRVS signal intensity decreases exponentially with increasing energy, data collected above this region (given our allocated beamtime) would have had a low signal-to-noise ratio.

Computational methods. DFT methods were used to simulate the NRVS spectra and Mössbauer parameters of all structural candidates, and to evaluate the hydrogen-atom abstraction reaction coordinates. Spin-unrestricted DFT calculations were performed using the Turbomole 6.3[30] and Gaussian 09[31] programs. Turbomole 6.3 was used to perform geometry optimizations and frequency calculations of the structural candidates in Supplementary Fig. 6, with the BP86[32–34] exchange-correlation functional and the double-ζ def2-SVP basis set[35]. Single-point energies were recomputed using the larger triple-ζ basis set def2-TZVP[35]. Turbomole calculations were expedited by expanding the Coulomb integrals in an auxiliary basis set, using the *RI*-J approximation[36,37]. Solvation effects were taken into account by using the conductor-like screening model (COSMO) method[38,39] with a dielectric constant $\varepsilon_r = 4$ as is appropriate for the protein environment (the COSMO radii were set as follows: H, 1.30 Å; C, 2.00 Å; N, 1.83 Å; O, 1.72 Å; Cl, 2.05 Å; Br, 2.16 Å; S, 2.16 Å; and Fe, 2.23 Å). This is referred to as the *RI*-BP86/def2-SVP (or def2-TZVP)/COSMO approach or level of theory.

Gaussian 09 was used to perform geometry optimizations and frequency calculations of the structural candidates $\mathbf{1_{Cpg}}$–X in Fig. 3, with the functional/basis set combination BP86/6-311G*[40–43]. Solvation effects were taken into account with the polarized continuum model (PCM)[44–47], using $\varepsilon = 4.0$. This is referred to as the BP86/6-311G*/PCM approach or level of theory.

NRVS PVDOS spectra were simulated by fitting the DFT-calculated mode composition factor[48]

$$e_{n,\mathrm{Fe}}^2 = \frac{m_{\mathrm{Fe}} r_{n,\mathrm{Fe}}^2}{\sum_i^{\mathrm{atoms}} m_i r_{n,i}^2}$$

(where m is the mass of atom i, and r is the displacement of atom i) for each normal mode n with individual Gaussians of FWHM 15 cm^{-1}, using the *gennrvs* script[49].

Mössbauer isomer shifts and quadrupole splittings were calculated according to published methods[50].

The initial structure of the SyrB2 Fe(II) active site used for DFT calculations was taken from its crystal structure (Supplementary Fig. 1 and ref. 19). Inclusion of the substrate (L-Cpg-SH, where the terminal –SH group represents truncation at the thioester linkage to the phosphopantetheine cofactor) was modelled according to ref. 12. Except where stated, the S atom of the substrate was frozen during geometry optimization. Note that the substrate does indeed fit well in the cavity of the active site (Supplementary Fig. 1d).

The O$_2$-reaction coordinate starting from the SyrB2–Cl Fe(II) active site was pursued analogously to ref. 24, at the *RI*-BP86/def2-SVP(def2-TZVP)/COSMO level of theory. The complete O$_2$-reaction coordinate for the L-Cpg-bound active site (with either Cl$^-$ or Br$^-$) is shown in Supplementary Fig. 4, and Supplementary Fig. 5 shows the final O–O cleavage step, leading to the Fe(IV)=O intermediate, for three versions of the active site containing L-Cpg (inert substrate), L-Thr (native substrate) and L-Nva (non-native substrate).

The hydrogen-atom abstraction reaction coordinates of the SyrB2–Cl Fe(IV)=O intermediate were evaluated using the Turbomole 6.3 program[30]. $\mathbf{1_{Thr}}$–Cl was optimized at the B3LYP[51–53]+D2/def2-SVP level (where +D2 stands for the second version of Grimme's empirical dispersion correction[54,55]). Thermodynamic corrections to give enthalpic (ΔH) and Gibbs (ΔG) energies were calculated at $T = 278.15$ K to reproduce experimental conditions[7]. Single-point energies were calculated at the B3LYP+D2/def2-TZVP/ COSMO($\varepsilon_r = 4.0$) level. The calculated NRVS spectra of these Thr-bound species (Supplementary Fig. 10) are similar to those of their L-Cpg-bound counterparts (Supplementary Fig. 6),

showing that the substrate does not affect the NRVS spectra because it is not directly coordinated to the Fe centre. Starting with $\mathbf{1_{Thr}}$–Cl and $\mathbf{2_{Thr}}$–Cl as the reactant complexes, each hydrogen-atom abstraction reaction was pursued along the oxo–H(L-Thr) coordinate and each transition state was optimized from the highest-energy structure along the reaction coordinate. An internal reaction coordinate was calculated from each optimized transition state (forward) to obtain the product (Fe(III)–OH + substrate radical) and (backward) to confirm the validity of the reactant complex structure.

30. Ahlrichs, R., Bär, M., Häser, M., Horn, H. & Kölmel, C. Electronic structure calculations on workstation computers: the program system Turbomole. *Chem. Phys. Lett.* **162**, 165–169 (1989).
31. Frisch, M. J. *et al.* Gaussian 09, Revision A.1 (Gaussian, Wallingford, 2009).
32. Becke, A. D. Density-functional exchange-energy approximation with correct asymptotic behavior. *Phys. Rev. A* **38**, 3098–3100 (1988).
33. Perdew, J. Density-functional approximation for the correlation energy of the inhomogeneous electron gas. *Phys. Rev. B* **33**, 8822–8824 (1986).
34. Vosko, S. H., Wilk, L. & Nusair, M. Accurate spin-dependent electron liquid correlation energies for local spin density calculations: a critical analysis. *Can. J. Phys.* **58**, 1200–1211 (1980).
35. Weigend, F. & Ahlrichs, R. Balanced basis sets of split valence, triple zeta valence and quadruple zeta valence quality for H to Rn: design and assessment of accuracy. *Phys. Chem. Chem. Phys.* **7**, 3297–3305 (2005).
36. Eichkorn, K., Treutler, O., Öhm, H., Häser, M. & Ahlrichs, R. Auxiliary basis sets to approximate Coulomb potentials. *Chem. Phys. Lett.* **240**, 283–290 (1995).
37. Eichkorn, K., Weigend, F., Treutler, O. & Ahlrichs, R. Auxiliary basis sets for main row atoms and transition metals and their use to approximate Coulomb potentials. *Theor. Chim. Acta* **97**, 119–124 (1997).
38. Klamt, A. & Schüürmann, G. COSMO: a new approach to dielectric screening in solvents with explicit expressions for the screening energy and its gradient. *J. Chem. Soc. Perkin Trans. 2* **0**, 799–805 (1993).
39. Schäfer, A., Klamt, A., Sattel, D., Lohrenz, J. C. W. & Eckert, F. COSMO implementation in Turbomole: extension of an efficient quantum chemical code towards liquid systems. *Phys. Chem. Chem. Phys.* **2**, 2187–2193 (2000).
40. Wachters, A. Gaussian basis set for molecular wavefunctions containing third-row atoms. *J. Chem. Phys.* **52**, 1033–1036 (1970).
41. Hay, P. J. Gaussian basis sets for molecular calculations. The representation of 3*d* orbitals in transition-metal atoms. *J. Chem. Phys.* **66**, 4377–4384 (1977).
42. McLean, A. D. & Chandler, G. S. Contracted Gaussian basis sets for molecular calculations. I. Second row atoms, *Z*=11–18. *J. Chem. Phys.* **72**, 5639–5648 (1980).
43. Krishnan, R., Binkley, J. S., Seeger, R. & Pople, J. A. Self-consistent molecular orbital methods. XX. A basis set for correlated wave functions. *J. Chem. Phys.* **72**, 650–654 (1980).
44. Mennucci, B. & Tomasi, J. Continuum solvation models: a new approach to the problem of solute's charge distribution and cavity boundaries. *J. Chem. Phys.* **106**, 5151–5158 (1997).
45. Mennucci, B., Cancès, E. & Tomasi, J. Evaluation of solvent effects in isotropic and anisotropic dielectrics and in ionic solutions with a unified integral equation method: theoretical bases, computational implementation, and numerical applications. *J. Phys. Chem. B* **101**, 10506–10517 (1997).
46. Cammi, R., Mennucci, B. & Tomasi, J. Second-order Møller−Plesset analytical derivatives for the polarizable continuum model using the relaxed density approach. *J. Phys. Chem. A* **103**, 9100–9108 (1999).
47. Cammi, R., Mennucci, B. & Tomasi, J. Fast evaluation of geometries and properties of excited molecules in solution: a Tamm-Dancoff model with application to 4-dimethylamino-enzonitrile. *J. Phys. Chem. A* **104**, 5631–5637 (2000).
48. Leu, B. M. *et al.* Quantitative vibrational dynamics of iron in nitrosyl porphyrins. *J. Am. Chem. Soc.* **126**, 4211–4227 (2004).
49. Tenderholt, A. gennrvs (2009); Pymol script available at http://www.stanford.edu/ group/solomon/gennrvs/gennrvs.py.txt.
50. Srnec, M. *et al.* Structural and spectroscopic properties of the peroxodiferric intermediate of *Ricinus communis* soluble Δ^9 desaturase. *Inorg. Chem.* **51**, 2806–2820 (2012).
51. Becke, A. D. Density-functional thermochemistry. III. The role of exact exchange. *J. Chem. Phys.* **98**, 5648–5652 (1993).
52. Lee, C., Yang, W. & Parr, R. Development of the Colle-Salvetti correlation-energy formula into a functional of the electron density. *Phys. Rev. B* **37**, 785–789 (1988).
53. Miehlich, B., Savin, A., Stoll, H. & Preuss, H. Results obtained with the correlation energy density functionals of Becke and Lee, Yang and Parr. *Chem. Phys. Lett.* **157**, 200–206 (1989).
54. Grimme, S. Accurate description of van der Waals complexes by density functional theory including empirical corrections. *J. Comput. Chem.* **25**, 1463–1473 (2004).
55. Grimme, S. Semiempirical GGA-type density functional constructed with a long-range dispersion correction. *J. Comput. Chem.* **27**, 1787–1799 (2006).